*Journal of Global Positioning Systems (2026)*
*Vol. 22, Issue 1: 18-31*
*DOI:10.5081/jgps.22.1.18*

# Flood Detection Using CYGNSS GNSS-R Observations - A Case Study of the 2022 Sindh Flood, Pakistan

**Afaq Karim(✉)[1,2], Dongkai Yang[1,2], Omada Friday Ojonugwa[2]**

1 School of Information and Communication Engineering, Beihang University, Beijing, China 100191

2 International Innovation Institute, Beihang University, Hangzhou, China 311115

✉ the corresponding author, afaqkarim@buaa.edu.cn

**Abstract**: Flood monitoring and mapping are essential for effective disaster response, particularly in regions frequently affected by extreme rainfall events. Conventional flood detection methods are often constrained by high costs, cloud cover, and limited temporal resolution. This study investigates the capability of Global Navigation Satellite System Reflectometry (GNSS-R) for flood detection using Level-1 data from the Cyclone Global Navigation Satellite System (CYGNSS) during the severe August 2022 flood event in Sindh Province, Pakistan. Surface reflectivity was estimated using a bistatic radar formula, in which the corrected signal-to-noise ratio (SNRc) was derived as a proxy for surface water presence after quality control, incidence-angle filtering, and outlier removal. To generate continuous flood reflectivity fields from irregular CYGNSS observations, a Natural Neighbor interpolation technique based on Voronoi tessellation was applied. Flooded areas were identified using an empirically derived SNRc threshold of approximately 16 dB, determined from observations over permanent water bodies. The resulting CYGNSS-derived flood maps show strong spatial agreement with MODIS-based flood inundation maps. The overall accuracy achieved is 0.819, indicating that approximately 82% of the MODIS and CYGNSS grid cells were correctly classified.

**Keywords**: CYGNSS, GNSS-Reflectometry, Flood Mapping, Remote Sensing

## 1. Introduction

Natural disasters pose significant challenges to communities and the environment, often resulting in severe disruptions that exceed the adaptive capacity of affected populations [1]. Among these, floods are recognized as one of the most destructive natural hazards, causing extensive damage to both the built and natural environments and leading to the displacement of human settlements [2]. Globally, the economic losses associated with flood disasters have risen substantially over recent decades [3]. Flooding typically occurs when rivers, lakes, dams, or dikes overflow their boundaries and inundate low-lying areas during periods of intense or prolonged rainfall. Furthermore, the increase in Earth's surface temperature contributes to higher evaporation rates, which in turn intensify overall precipitation. This escalation in precipitation not only heightens the likelihood of inland flooding but also amplifies the risk of coastal inundation [4].

Land surveying and airborne observations have traditionally been employed for flood detection; however, these methods become costly and time-consuming when applied over large spatial scales. Space-based remote sensing (RS) has emerged as a

**Editor-In-Charge: Dr. Xiufeng He**
**Dr. Minfeng Song**

practical and efficient alternative, offering timely and wide-area observations through various satellite-borne sensors. Nevertheless, certain limitations persist in the application of RS data products for flood monitoring. For instance, optical RS systems are constrained by weather conditions, rendering them ineffective during heavy cloud cover or nighttime [5]. In contrast, radar-based RS operating in the microwave spectrum can overcome these challenges, as radar waves penetrate clouds and vegetation and can acquire data regardless of daylight or weather conditions. Among the radar sensors currently in operation, Synthetic Aperture Radar (SAR) provides high spatial resolution imagery based on a monostatic configuration [6] [7]. However, the revisit time of monostatic SAR satellites typically exceeding one week limits their capacity to capture the rapid temporal dynamics of flood events. Therefore, despite their accuracy, SAR images are not routinely used for near-real-time operational flood monitoring due to insufficient temporal resolution [8] [9].

In situ observations of surface water are usually collected as point measurements during field work or after floods have ended, but these data are difficult to collect regularly. Consequently, satellite remote sensing is widely used to map surface water. Optical indices can map open water well, but they often miss water under vegetation and show large differences in wetlands [10] [11]. Optical data are also limited by cloud cover, especially during extreme weather events. Microwave sensors, including radiometers and radar, are less affected by clouds and can detect water through some vegetation, and they have been used for flood mapping for many years [12] [13]. However, radiometer products such as GIEMS-2 and SWAMPSv3 have coarse spatial resolution (>25 km) [14] [15], while radar systems like Sentinel-1 provide much finer detail but revisit the same area less often (>1 week) [16] [17].

Numerous scientific applications of Global Navigation Satellite System (GNSS) have been developed in recent decades, including GNSS-based remote sensing [18] [19]. GNSS signals reflected from the Earth's surface carry information regarding the physical and dielectric characteristics of the reflecting surface. These reflections have been successfully applied to study a range of geophysical and hydrological parameters, including snow depth [20], ice height and sea level [21], soil moisture [22], vegetation dynamics [23], flooding [24, 25], ocean eddies [26], wind speed [27] [28], and salinity [29].

Global Navigation Satellite System Reflectometry (GNSS-R) is an efficient form of microwave remote sensing. A constellation of small GNSS-R satellites can offer significantly shorter revisit times and extensive spatial coverage at a fraction of the cost of conventional remote sensing missions. Numerous prior studies have demonstrated the successful application of GNSS-R technology for monitoring the oceans, land surfaces, and ice [30-33]. Microwave signals are influenced by several surface and environmental parameters, including soil moisture, surface roughness, vegetation, and topography [34]. Similarly, GNSS-R signals, operating under a bistatic radar configuration, are also affected by these factors. However, GNSS signals operate in the L-band frequency, which is particularly suitable for soil moisture and surface water remote sensing because of its greater ability to penetrate vegetation compared to shorter microwave wavelengths [22]. Furthermore, the bistatic geometry used in GNSS-R exhibits reduced sensitivity to surface roughness relative to monostatic radar systems [35].

In this study, we implement flood detection using CYGNSS GNSS-R data. Although CYGNSS has a low spatial resolution, it offers higher temporal resolution and can collect data even during intense storms and heavy cloud cover conditions when other data sets such as SAR acquisitions are often limited by long revisit times or scheduling constraints.

## 2. Data Set Description

### 2.1 Study Area

The Sindh Province has a dense population, as well as extensive agricultural and urban landscapes. Sindh is traversed by the Indus River, Pakistan's longest river, extending approximately 3,180 km (1,976 miles) from its source in Gilgit–Baltistan to its

delta at the Arabian Sea, near Karachi (Fig. 1) [36]. In July 2022, the southern and central regions of Sindh experienced intense monsoonal rainfall, resulting in significant flooding across several urban centers. Although the situation remained relatively stable through the end of July with only localized flooding in southern and coastal districts, the persistent precipitation saturated the soil, substantially reducing its infiltration capacity. Consequently, when consecutive heavy rainfall events occurred during August (Fig. 2), combined with a medium-scale flood in the Indus River between the 11th and 27th of August, the situation deteriorated rapidly across the province. By late August, the rainfall had largely subsided; however, the cumulative and downstream impacts of the earlier precipitation continued well into September. The inflow of large volumes of runoff water from neighboring Baluchistan further exacerbated the crisis, overwhelming the drainage infrastructure and causing widespread devastation, particularly in the left-bank districts of Sindh [37].

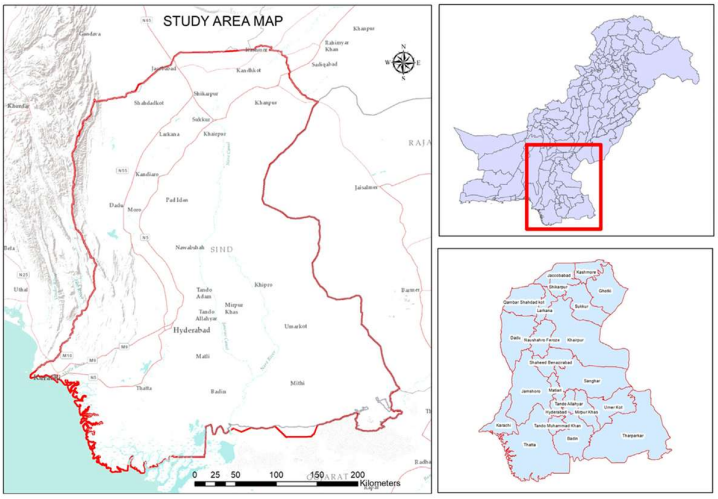


Fig. 1 Map of the study area showing the Sindh province of Pakistan [36].

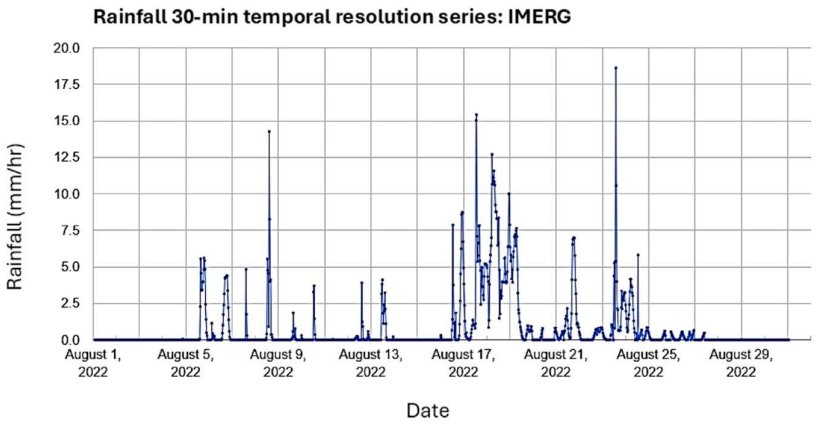


Fig. 2 GPM-IMERG rainfall estimates at Sindh Province in August 2022 [36]

The period of 30–31 August 2022 was selected because it corresponds to the peak flooding stage in Sindh Province, during which surface inundation was most extensive. In addition to the results presented in the manuscript, the proposed algorithm was also tested over an extended period from 29 August to 4 September 2022. The analysis over this longer duration produced no significant changes in the spatial flood patterns or SNRc–based inundation estimates, indicating that the results obtained for 30–31 August

are representative and stable. However, processing the extended dataset substantially increased computational time and data handling requirements due to the large volume of CYGNSS observations, without providing additional insight beyond the peak-flood analysis. For these reasons, and to maintain clarity and computational efficiency, the manuscript focuses on the peak flood dates, which provide the most informative and impactful validation of the proposed methodology.

### 2.2 CYGNSS Data

The CYGNSS mission comprises a constellation of eight microsatellites, each equipped with a GNSS-R receiver capable of tracking and processing four GPS signals simultaneously. Reflected GPS L1 C/A signals from the Earth's surface are used to generate Delay Doppler Maps (DDMs), which form the basis for geophysical parameter retrieval. The CYGNSS constellation achieves a median revisit time of approximately 2.8 hours and a mean revisit time of 7.2 hours, enabling frequent temporal coverage of dynamic surface processes [38]. The theoretical footprint of the specular reflection observed by CYGNSS is approximately 0.5 km × 0.5 km, while over oceanic surfaces characterized by higher roughness, the effective spatial resolution is around 25 km × 25 km [39] [40].

CYGNSS generates four levels of publicly available data products, managed by the CYGNSS Science Operations Center. These products range from Level 0 to Level 3, with Levels 1, 2, and 3 provided in Network Common Data Form (NetCDF).

In this study, we utilized Level-1 (L1) Version 3.2 data from the CYGNSS mission, representing the lowest-level geophysical data product available. The dataset is provided in NetCDF format, containing daily observations recorded by each of the eight CYGNSS microsatellites. Consequently, up to eight individual NetCDF files correspond to each Day of Year (DOY), collectively offering comprehensive temporal coverage. The L1 dataset is freely accessible through NASA's Jet Propulsion Laboratory (JPL) Physical Oceanography Distributed Active Archive Center (PO.DAAC) at https://podaac.jpl.nasa.gov. The variables extracted include specular point coordinates, SNR, incidence angle, transmit power, transmitter and receiver antenna gains, and signal path lengths

### 2.3 MODIS Data

Moderate-Resolution Imaging Spectroradiometer (MODIS) is an advanced sensor aboard NASA's Terra and Aqua spacecraft, designed to gather data across a broad spectrum of electromagnetic waves. Together, the Terra and Aqua MODIS sensors cover the Earth's entire surface every one to two days. The sensors measure 36 spectral bands ranging from 0.405 μm to 14.385 μm. The data is released at three different spatial resolutions: 250 meters (bands 1–2), 500 meters (bands 3–7), and 1000 meters (bands 8–36). MODIS data, accessible at https://modis.gsfc.nasa.gov, is used for a significant number of land, atmospheric, and oceanic applications [38].

In this study, MODIS imagery was employed to validate the flood maps generated using CYGNSS observations. Sindh Province was defined as the area of interest using GAUL 2015 administrative boundaries, and permanent water bodies were identified from the MODIS MOD44W water mask to establish a baseline reference. Floodwater detection was carried out using MODIS Surface Reflectance MOD09GA data from late August 2022, where the Modified Normalized Difference Water Index (MNDWI) was computed to enhance open-water features.

## 3. Data Pre-processing and Methodology

### 3.1 Data Filtering

Data were filtered to mitigate noise and remove outliers. Coherent reflections become sensitive when incidence angles exceed 40–50° and are negligible for this study's objectives [39]; therefore, all observations with incidence angles >65° were excluded as show in Fig. 6. The Level-1A data product used in this study was refined by applying a set of quality control flags designed and included in the data to indicate potential problems [38]. The specific flags used were 2 (S-band

transmitter powered up), 4 (spacecraft attitude error), 5 (blackbody DDM), 8 (DDM is a test pattern), 16 (direct signal present in the DDM), and 17 (low confidence in the GPS EIR estimate). Measurements with SNR < 2 dB and with CYGNSS antenna gain < 0 dB or > 13 dB were also discarded. These thresholds are empirical rather than standardized but have been shown to improve retrieval quality in practice [22].

Tab.1 CYGNSS data Parameters used in this study.

| CYGNSS Parameters | Description |
|---|---|
| ddm_snr | Delay Doppler Map (DDM) signal-to-noise ratio, in dB. |
| gps_ant_gain_db_i | GPS transmit antenna gain in dBi. |
| gps_tx_power_db_w | GPS transmit power, in dB. |
| rx_to_sp_range | Distance between the CYGNSS satellite and the specular point in meters. |
| tx_to_sp_range | Distance between the GPS satellite and the specular point in meters. |
| sp_lat | Specular point latitude, in degrees North. |
| sp_lon | Specular point longitude, in degrees East. |
| sp_rx_gain | The receive antenna gains in the direction of the specular point, in dBi. |
| quality_flags | Per-DDM quality flags. |
| sp_inc_angle | The specular point incidence angle, in degrees. |

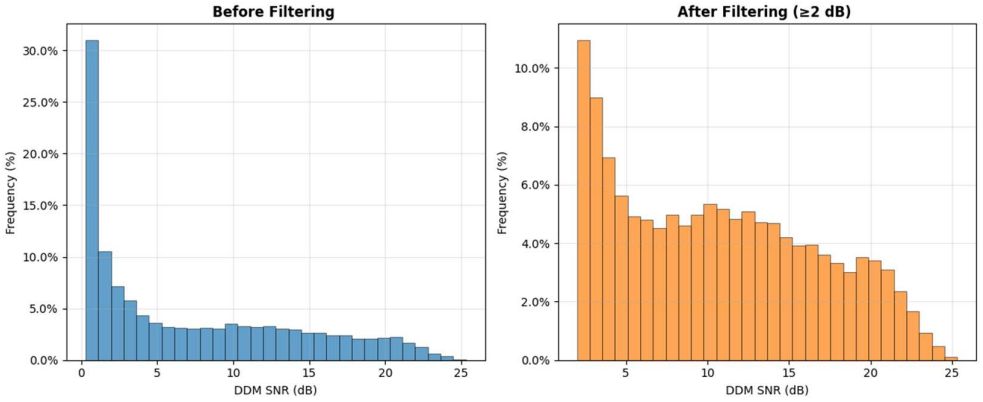


Fig. 3 CYGNSS observations before and after filtering DDM SNR

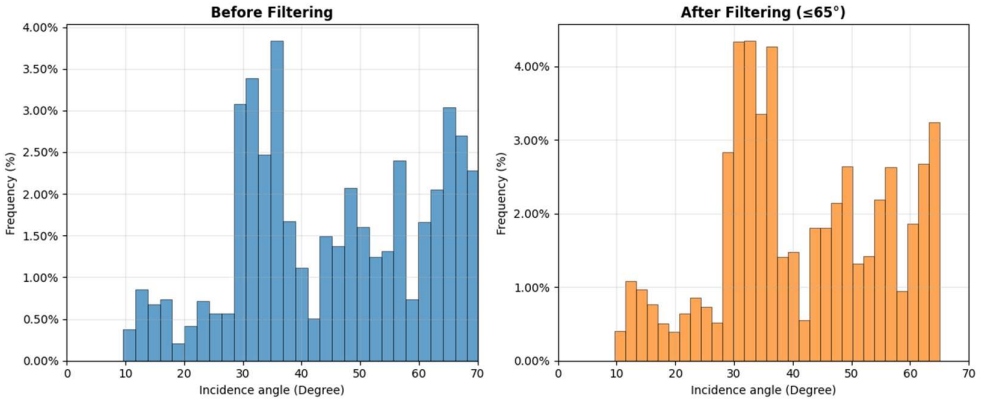


Fig. 4 CYGNSS observations before and after filtering Incidence Angle.

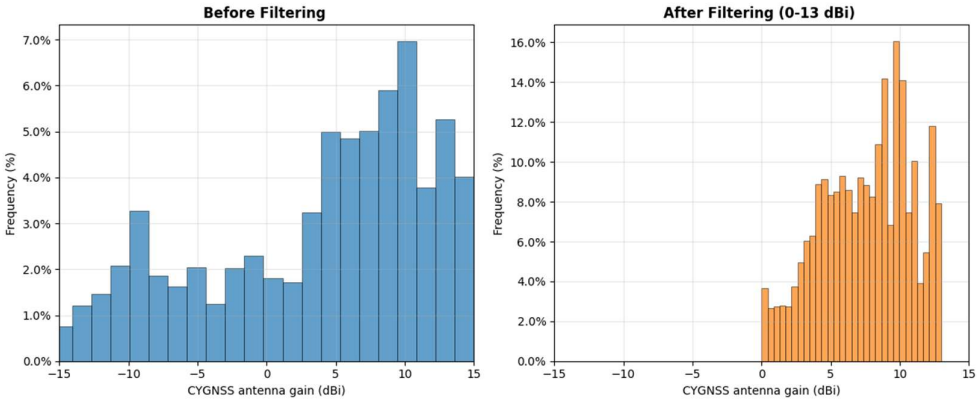


Fig. 5 CYGNSS observations before and after filtering Receiver Antenna Gain

A total of 54 CYGNSS Level-1 NetCDF (.nc) files were processed. After applying quality-control filtering, 7,396,543 specular point reflections remained. Following additional technical filtering criteria, this number was reduced to 4,180,565 specular point reflections. Finally, after spatial filtering to retain only observations within Sindh Province, 11,722 specular point reflections were used in the flood analysis

### 3.2 Bistatic Radar Equations

The CYGNSS and GPS constellations together realize a bistatic radar architecture. GPS spacecraft transmit circularly polarized microwave signals, which are forward-scattered by the Earth's surface and subsequently received by the CYGNSS GNSS-reflectometry payloads. The scattered fields encode information about the electromagnetic and geometric properties of the reflecting surface. The reflections from inland water bodies are dominated by the coherent part and can be detected by CYGNSS due to their smoother, more specular behavior relative to surrounding land [41] [42]. As the reflections from inland water bodies are dominated by the coherent part [43], the peak coherent scattered power is defined as [31] [32]:

$$P_{RL}^{coh} = \frac{P_R^t G^t G^r}{(d_{ts}+d_{sr})^2}\left(\frac{\lambda}{4\pi}\right)\Gamma_{RL} \qquad (1)$$

where $P_{RL}^{coh}$ is the peak value of coherently received power, R denotes the right-handed circular polarization (RHCP) of the GPS transmit antenna, and L is related to the left-handed circular polarization (LHCP) of forward-scattered signals collected by the downward-looking antenna. $P_R^t$ is the transmitted power, $G^t$is the gain of the transmitter antenna, $G^r$is the gain of the receiver antenna, λ is the GPS L1 wavelength (≈0.19m), and $d_{ts}$ is the distance between the specular reflection point and the GPS transmitter. Similarly, $d_{sr}$ is the distance between the specular reflection point and the GNSS-R receiver, and $\Gamma_{RL}$ is the surface reflectivity.

In addition to the mentioned parameters, $P_{RL}^{coh}$ is also affected by system noise. Therefore, the signal-to-noise ratio (SNR) can be defined as:

$$SNR = \frac{P_{RL}^{coh}}{N} = \frac{P_R^t G^t G^r}{(d_{ts}+d_{sr})^2}\left(\frac{\lambda}{4\pi}\right)^2 \frac{\Gamma_{RL}}{N} \qquad (2)$$

where $N$ is the noise value. Since the magnitude of the SNR is not equal to the reflected power, the surface reflectivity SR can be empirically estimated using,

$$SR = SNR_c \propto SNR\left(\frac{(d_{ts}+d_{sr})^2}{P_R^t G^t G^r}\right)\left(\frac{4\pi}{\lambda}\right)^2 \qquad (3)$$

Finally, the SR in dB is:

$$SR = SNR_{\boldsymbol{cdB}} \propto SNR_{\boldsymbol{dB}} + 10\log\left(\left(\frac{(d_{ts}+d_{sr})^2}{P_R^t G^t G^r}\right)\left(\frac{4\pi}{\lambda}\right)^2\right) \qquad (4)$$

$SNR_{\boldsymbol{cdB}}$ representing the corrected signal to ratio (c represents corrected) is strongly related to the hydrological conditions of the land [18] [24] and all the other parameters in the above equation are obtained from the CYGNSS data.

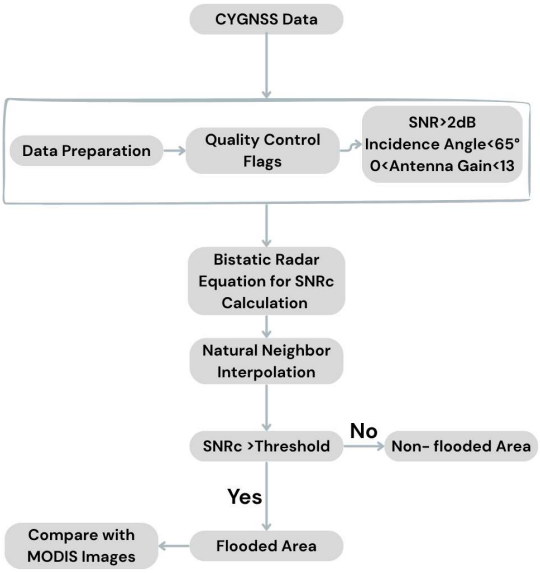


Fig. 6 Overall workflow Diagram.

### 3.3 Natural Neighbor Interpolation

To generate a continuous spatial representation of the CYGNSS-derived signal-to-noise ratio (SNRc) values across Sindh Province, a Natural Neighbor interpolation technique was applied (Fig. 7). This method was selected for its ability to produce smooth and physically realistic surfaces from irregularly distributed satellite observation points without introducing artificial extrema. An interpolation grid with a spatial resolution of 0.1° was established to cover the entire Sindh region. The Natural Neighbor algorithm determines each interpolated value by calculating a weighted average of neighboring data points based on their proportional Voronoi cell overlap, ensuring local accuracy and continuity between observations.

The principal formula is [44]

$$G(x,y) = \sum_{i=1}^{N} w_i f(x_i, y_i) \qquad (5)$$

where G is the estimated value at $(x,y)$, $w_i = \frac{Q_k}{R_k}$ are the weights and $f(x_i,y_i)$is the known data at $(x_i,y_i)$, $R_k$ is the area of the initial Voronoi diagram element for point $P_k = (x_i,y_i)$. $Q_k$ is the intersection area of $R_k$ and newly constructed element for the point $(x,y)$. Therefore, this algorithm functions by inserting an additional point into the existing Voronoi diagram..

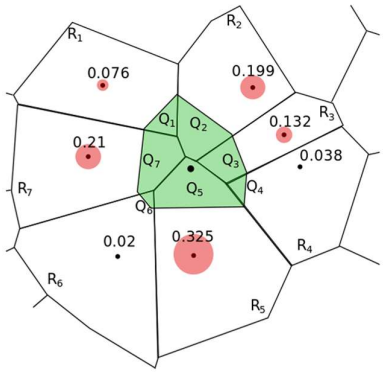


Fig. 7 Natural neighbor interpolation method.

The areas of the colored circles represent the interpolating weights, and the shaded region denotes the new Voronoi element constructed for the point to be interpolated [44].

## 4. Results Analysis and Validation

### 4.1 Results Analysis

The spatial distribution of SNRc across Sindh Province during 30–31 August 2022, coinciding with the peak flooding period, is provided in Fig. 8. The original SNRc values in Fig. 8(a) reveal extensive areas of elevated signal strength, with values exceeding 16 dB, indicative of strong GNSS-R reflections associated with widespread surface water inundation caused by monsoonal flooding. A comparable spatial pattern is observed in the interpolated SNRc derived from CYGNSS data in Fig. 8(b), which preserves the dominant flood-related features present in the original observations. In contrast, regions characterized by lower SNRc values correspond to areas with little or no flooding. The strong spatial coherence between the original and interpolated SNRc fields confirms the reliability of the interpolation approach and further demonstrates the sensitivity of GNSS-R backscatter measurements to flood-induced surface water.

The spatial distribution of SNRc values prior to the onset of monsoonal flooding, during the third week of June 2022, is provided in Fig. 9(a–b) and represents baseline pre-flood conditions across Sindh Province.

Both the original and interpolated SNRc fields exhibit generally low backscatter intensity, with values predominantly ranging between 10 and 15 dB. This spatial pattern is characteristic of dry surface conditions over most of the province. Slightly elevated SNRc values are observed in coastal regions, likely reflecting naturally moist or saline soils. The absence of pronounced high-SNRc clusters confirms the lack of significant surface water during this period.

The statistical behavior of SNRc under non-flood conditions is further illustrated by the June histogram in Fig. 10, which exhibits a unimodal distribution centered at approximately 11 dB. This distribution reflects the low surface reflectivity typical of dry land surfaces. In contrast, the August data histogram provided in Fig. 11 shows a pronounced rightward shift, with the mean SNRc increasing to around 18 dB. This shift indicates a substantial enhancement in surface reflectivity, consistent with the widespread presence of standing water during the flood period.

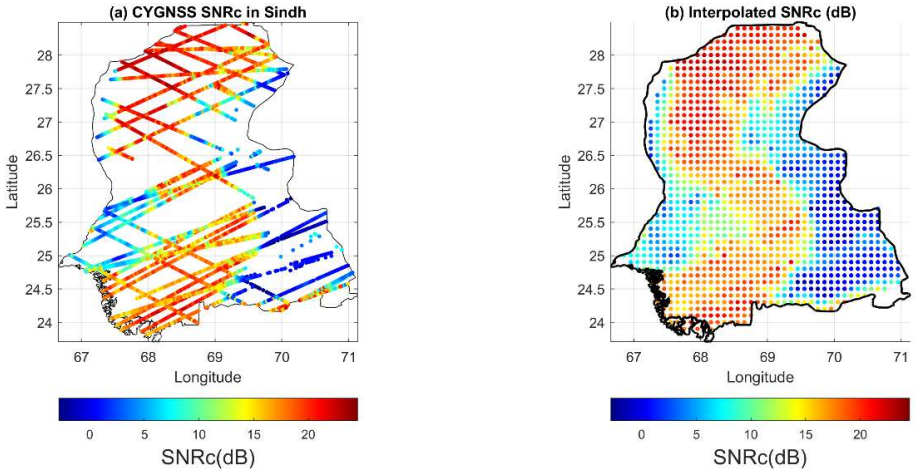


Fig. 8 (a) CYGNSS SNRc observations in Sindh (b) Interpolated CYGNSS SNRc in Sindh for 30-31 August 2022.

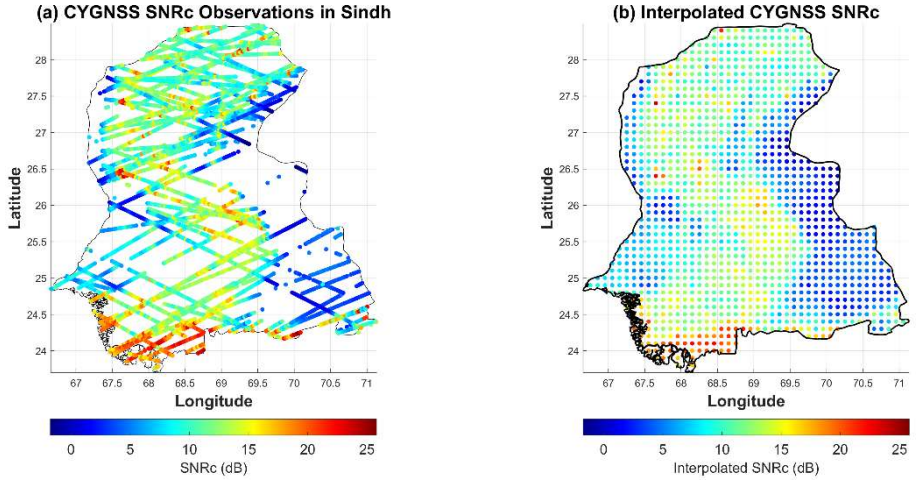


Fig. 9 (a) CYGNSS SNRc observations in Sindh (b) Interpolated CYGNSS SNRc in Sindh before flooding.

To calculate the flood inundation areas using SNRc, a simple threshold was used to distinguish flood from non-flood locations. The SNRc threshold of 16 dB was determined empirically based on observations over known permanent water bodies within the study area. The statistical distribution of CYGNSS SNRc measurements over permanent water bodies was analyzed for June 2022 data. The mean

SNRc value over permanent water bodies was found to be approximately 16 dB, with most values exceeding this level during inundation conditions.

It is important to emphasize that this threshold is region-specific and its transferability to other geographical areas with different land cover, climate, or hydrology cannot be assumed without re-evaluation. At L-band, GNSS-R signals are sensitive to surface roughness and vegetation density. Dense vegetation can attenuate the reflected signal, potentially reducing SNRc over inundated areas and causing underestimation if the threshold is set too high. Conversely, rough soil surfaces in sparsely vegetated zones can reduce coherent reflection, leading to lower SNRc even in non-flooded conditions, which may contribute to overestimation when a fixed low threshold is applied.

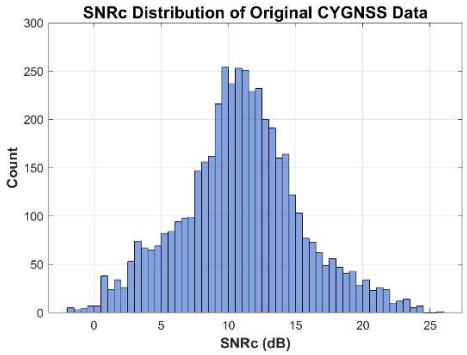


Fig. 10 Distribution of SNRc for June 2022

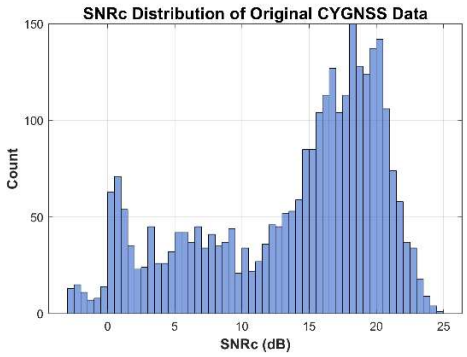


Fig. 11 Distribution of SNRc for August 2022

The contrast between flood and non-flood months, as evident from the histogram distributions, further supports the selection of an SNRc threshold for flood detection. During non-flood periods, most CYGNSS SNRc observations fall within the range of 5–15 dB, whereas during flood conditions the majority of values lie between 15 and 22 dB.

### 4.2 Results Validation

The spatial comparison between flood extent derived from CYGNSS GNSS-R observations and MODIS imagery across Sindh Province is provided in Fig. 12(a). The MODIS flood map serves as the reference dataset for validating the GNSS-R–based flood detection results. The CYGNSS SNRc field is shown with MODIS-identified flooded areas overlaid in red, allowing a direct visual assessment of their correspondence. A strong spatial agreement is observed, with regions of elevated SNRc values largely coinciding with MODIS flood zones, indicating that CYGNSS successfully captured the major inundated areas during the flood event.

A more detailed comparison between CYGNSS-detected flood points and MODIS flood boundaries is shown in Fig. 12(b). While most of the MODIS-identified flood extent is well represented in the CYGNSS results, additional high-SNRc zones are detected in the southern parts of Sindh, which are attributed to naturally moist or saline soils rather than flood inundation. Conversely, some narrow riverine corridors and south-eastern flooded regions identified by MODIS are not captured by CYGNSS. This discrepancy arises from the absence of specular reflection observations in those areas, rather than from limitations in the flood detection methodology itself. The resulting spatial gaps reflect the irregular ground-track geometry of the CYGNSS constellation, which leads to non-uniform sampling density across the study region.

To quantitatively assess the flood detection capability of the CYGNSS derived product, a grid-based binary classification was performed against the MODIS flood reference dataset. Both datasets were aggregated to a common 0.1° × 0.1° grid covering the Sindh region. For CYGNSS, a binary flood mask was defined using the SNRc threshold of 16 dB. The MODIS flood polygons were rasterized onto the same grid to produce a reference binary mask.

The validation results demonstrate substantial agreement between the CYGNSS flood map and the MODIS reference. The overall accuracy obtained is 0.819, indicating that approximately 82% of the grid cells were correctly classified. The recall (sensitivity) of 0.871 obtained shows that the CYGNSS method detected nearly 87% of the flood area mapped by MODIS, confirming a strong capability to capture the main inundated zones. The precision of 0.671 reflects that about 67% of the cells flagged as flooded by CYGNSS were confirmed by MODIS; the remaining 33% represent overestimation relative to the reference due to the naturally moist or saline soils rather than flood inundation detected in the southern parts of Sindh. The F1 score, which balances recall and precision, is 0.758, indicating a robust overall performance.

The observed spatial changes also align closely with the Provisional Disaster Management Authority (PDMA) Sindh [37] flood-extent map in Fig. 13. Areas showing the strongest SNRc increases coincide with the darkest blue flood zones in the PDMA map

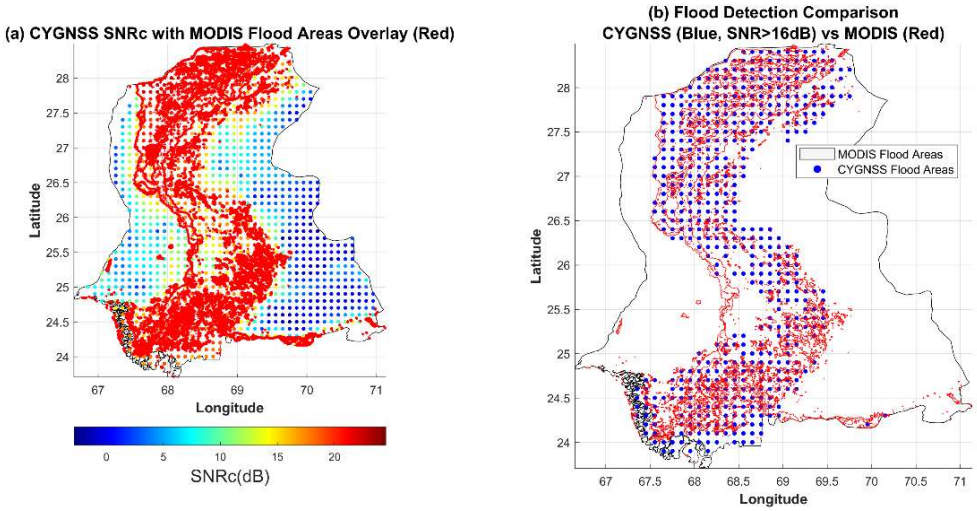


Fig. 12 (a) Spatial comparison between flood detection results derived from CYGNSS GNSS-R observations and MODIS. (b) Direct comparison between CYGNSS-detected flood points and MODIS flood boundaries.

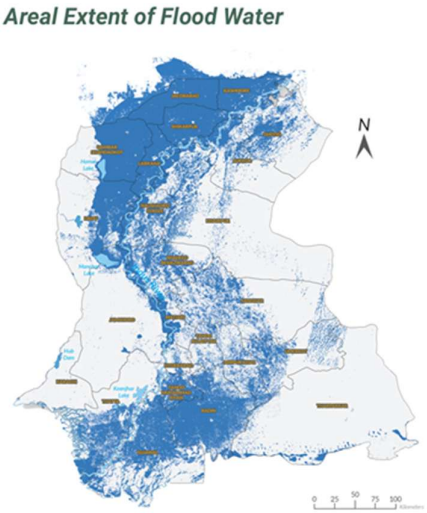


Fig. 13 Provisional Disaster Management Authority (PDMA) Sindh [37] flood-extent map.

Collectively, these findings validate the potential of GNSS-R observations for near-real-time flood detection and monitoring. The agreement between CYGNSS-derived SNRc patterns, MODIS imagery and PDMA's satellite-based flood mapping highlights the robustness of microwave reflectometry for hydrological assessment, particularly in regions with persistent cloud cover where optical sensors face limitations. This consistency also suggests that GNSS-R can serve as a complementary data source to traditional optical and radar-based flood monitoring systems, providing improved temporal resolution for capturing dynamic flood events.

However, the relatively coarse spatial resolution of CYGNSS data limits the detection of small or narrow inundation features, and vegetation or surface roughness can introduce minor reflectivity biases.

Integrating CYGNSS data with higher-resolution sensors such as Sentinel-1 or MODIS could further enhance spatial precision and support improved hydrological modeling.

## 5 Conclusion

This study demonstrated that the corrected Signal-to-Noise Ratio (SNRc) derived from CYGNSS GNSS-R data can reliably map flood inundation. The preprocessing steps removed low-quality observations, and the inverse bistatic radar equation was applied to compute SNRc, which was then interpolated onto a 0.1° grid. A threshold of 16 dB was empirically identified to distinguish flooded from non-flooded areas in Sindh, Pakistan. Validation against MODIS imagery yielded an overall accuracy of 0.819, confirming the effectiveness of the approach. The results highlight the sensitivity of GNSS-R backscatter to surface water and underscore its utility for operational flood monitoring, especially under cloudy conditions where optical sensors are limited. Future work should focus on integrating GNSS-R with higher resolution radar and optical data (e.g., Sentinel-1, MODIS) to refine detection accuracy and develop automated algorithms applicable to other flood prone regions.

## 6 References


[1] C. V. Westen, "Remote sensing for natural disaster management," in ISPRS 2000 congress: geoinformation for all, Amsterdam, 2000.

[2] R. O. Salami, J. K. V. Meding and H. Giggins, "Vulnerability of human settlements to flood risk in the core area of Ibadan metropolis, Nigeria," Journal of Disaster Risk Studies, vol. 9, no. 1, 2017.

[3] K. Ahmed, "Integrated Flood Risk Management in Asia; A Primer. ADPC; UNDP,2005.," Bangkok, Thailand, 2005.

[4] J. Houston, "Variability of precipitation in the Atacama Desert: its causes and hydrological impact," International Journal of Climatology, vol. 26, no. 15, pp. 2181 - 2198, 2006.

[5] P. A. Brivio, R. Colombo, M. Maggi and R. Tomasoni, "Integration of remote sensing data and GIS for accurate mapping of flooded areas," International Journal of Remote Sensing, vol. 23, no. 3, pp. 429-441, 2002.

[6] B. A. Hailegiorgis, D. Yang, X. Hong and L. Aung, "Analysis of CYGNSS Soil Moisture Retrieval Based on ANN over a Selected Region in Ethiopia," Journal of Global Positioning Systems, vol. 19, pp. 56-65, 2023.

[7] R. Oberstadler, H. Honsch and D. Huth, "Assessment of the mapping capabilities of ERS-1 SAR data for flood mapping: a case study in Germany," Hydrological Processes, vol. 11, no. 10, pp. 1415-1425, 1997.

[8] C. Kuenzer, H. Guo, J. Huth, P. Leinenkugel, X. Li and S. Dech, "Flood Mapping and Flood Dynamics of the Mekong Delta: ENVISAT-ASAR-WSM Based Time Series Analyses," Remote Sensing, vol. 5, no. 2, pp. 687-715, 2013.

[9] C. Chew, J. T. Reager and E. Small, "CYGNSS data map flood inundation during the 2017 Atlantic hurricane season," Scientific Reports, vol. 8, no. 1, p.9336, 2018.

[10] G. Lefebvre, A. Davranche, L. Willm, J. Campagna, L. Redmond, C. Merle, A. Guelmami and B. Poulin, "Introducing WIW for Detecting the Presence of Water in Wetlands with Landsat and Sentinel Satellites," Remote Sensing, vol. 11, no. 19, p. 2210, 2019.

[11] T. Nakaegawa, "Comparison of Water-Related Land Cover Types in Six 1-km Global Land Cover Datasets," Hydrology in Earth System Science and Society (HESSS), 2012.

[12] C. Prigent, E. Matthews, F. Aires and W. B. Rossow, "Remote sensing of global wetland dynamics with multiple satellite data sets," Geophysical Research Letters, vol. 28, no. 24, pp. 4631-4634, 2001.

[13] R. Schroeder, K. C. McDonald, B. D. Chapman, K. Jensen, E. Podest, Z. D. Tessler, T. J. Bohn and R.Zimmermann, "Development and Evaluation of a Multi-Year Fractional Surface Water Data Set Derived from Active/Passive Microwave Remote Sensing Data," Remote Sensing, vol. 7,

no. 12, 2015.

[14] C. Prigent, C. Jimenez and P. Bousquet, "Satellite-Derived Global Surface Water Extent and Dynamics Over the Last 25 Years (GIEMS-2)," Journal of Geophysical Research, vol. 125, no. 3, p. e2019JD030711, 2020.

[15] K. Jensen and K. Mcdonald, "Surface Water Microwave Product Series Version 3: A Near-Real Time and 25-Year Historical Global Inundated Area Fraction Time Series From Active and Passive Microwave Remote Sensing," IEEE Geoscience and Remote Sensing Letters, vol. 16, no. 9, pp. 1402-1406, 2019.

[16] J. Muro, M. Canty, K. Conradsen, C. Hüttich, A. A. Nielsen, H. Skriver, F. Remy, A. Strauch, F. Thonfeld and G. Menz, "Short-Term Change Detection in Wetlands Using Sentinel-1 Time Series," Remote Sensing, vol. 8, no. 10, p.795, 2016.

[17] V. Tsyganskaya, S. Martinis, P. Marzahn and R. Ludwig, "Detection of Temporary Flooded Vegetation Using Sentinel-1 Time Series Data," Remote Sensing vol. 10, no. 8, 2018.

[18] M. Rajabi, H. Nahavandchi and M. Hoseini, "Evaluation of CYGNSS Observations for Flood Detection and Mapping during Sistan and Baluchestan Torrential Rain in 2020," Water, vol. 12, no. 7, p. 2047, 2020.

[19] M. Rajabi, A. Amiri-Simkooei, H. Nahavandchi and V. Nafisi, "Modeling and Prediction of Regular Ionospheric Variations and Deterministic Anomalies," Remote Sensing, vol. 12, no. 6, p. 936, 2020.

[20] S. Tabibi, "Snow Depth and Soil Moisture Retrieval Using SNR-Based GPS and GLONASS Multipath Reflectometry.," Ph.D. Thesis, University of Luxembourg, 2016.

[21] W. Li, E. Cardellach, F. Fabra, A. Rius, S. Ribó and M. Martín-Neira, "First spaceborne phase altimetry over sea ice using TechDemoSat-1 GNSS-R signals," Geophysical Research Letters, vol. 44, no. 16, pp. 8369-8376, 2017.

[22] C. C. Chew and E. E. Small, "Soil Moisture Sensing Using Spaceborne GNSS Reflections: Comparison of CYGNSS Reflectivity to SMAP Soil Moisture," Geophysical Research Letters, vol. 45, no. 9, pp. 4049-4057, 2018.

[23] X. Wu, Y. Li and J. Xu, "Theoretical study on GNSS-R vegetation biomass," in IEEE International Geoscience and Remote Sensing Symposium (IGARSS), Munich, Germany, 2012.

[24] W. Wan, B. Liu, Z. Zeng, X. Chen, G. Wu, L. Xu, X. Chen and Y. Hong, "Using CYGNSS Data to Monitor China's Flood Inundation during Typhoon and Extreme Precipitation Events in 2017," Remote Sensing, vol. 11, no. 7, p. 854, 2019.

[25] Q. Yan, S. Jin, Y. Chen, Y. Jia and W. Huang, "Enhanced Hierarchical Vision Transformer Approach for Soil Moisture Retrieval Leveraging CYGNSS Data," in IEEE International Symposium on Geoscience and Remote Sensing (IGARSS), 2025.

[26] M. Hoseini, M. Asgarimehr, V. Zavorotny, H. Nahavandchi, C. Ruf and J. Wickert, "First Evidence of Mesoscale Ocean Eddies Signature in GNSS Reflectometry Measurements," Remote Sensing, vol. 12, no. 3, p. 542, 2020.

[27] M. P. Clarizia and C. S. Ruf, "Wind speed retrieval algorithm for the Cyclone Global Navigation Satellite System (CYGNSS) mission," IEEE Transactions on Geoscience and Remote Sensing, vol. 54, no. 8, pp. 4419-4432, 2016.

[28] X. Qiao, Q. Yan and W. Huang, "Hybrid CNN-Transformer Network With a Weighted MSE Loss for Global Sea Surface Wind Speed Retrieval From GNSS-R Data," IEEE Transactions on Geoscience and Remote Sensing, vol. 63, pp. 1-1, 2025.

[29] B. Liu, W. Wan and Y. Hong, "Can the Accuracy of Sea Surface Salinity Measurement Be Improved by Incorporating Spaceborne GNSS-Reflectometry?," IEEE Geoscience and Remote Sensing Letters, vol. 18, no. 1, pp. 3-7, 2021.

[30] Q. Yan, S. Liu, T. Chen, S. Jin, T. Xie and W.

Huang, "Mapping Surface Water Fraction Over the Pan-Tropical Region Using CYGNSS Data," IEEE Transactions on Geoscience and Remote Sensing, vol. 62, pp. 1-14, 2024.

[31] V. U. Zavorotny, S. Gleason, E. Cardellach and A. Camps, "Tutorial on Remote Sensing Using GNSS Bistatic Radar of Opportunity," IEEE Geoscience and Remote Sensing Magazine, vol. 2, no. 4, pp. 8-45, 2014.

[32] O. Eroglu, M. Kurum, D. Boyd and A. C. Gurbuz, "High spatio-temporal resolution CYGNSS soil moisture estimates using artificial neural networks," Remote Sensing, vol. 11, no. 19, p. 2272, 2019.

[33] P. J. G. Teunissen and O. Montenbruck, Springer Handbook of Global Navigation Satellite Systems, Springer, 2017.

[34] L. Guerriero, N. Pierdicca, A. Egido, M. Caparrini, S. Paloscia, E. Santi and N. Floury, "Modeling of the GNSS-R signal as a function of soil moisture and vegetation biomass," in IEEE International Geoscience and Remote Sensing Symposium (IGARSS), Melbourne, VIC, Australia, 2013.

[35] D. Masters, P. Axelrad and S. Katzberg, "Initial results of land-reflected GPS bistatic radar measurements in SMEX02," Remote Sensing of Environment, vol. 92, pp. 507-520, 2004.

[36] M. Usmania, H. M. T. Bhatti, R. Nanni, F. Bovolo and M. Napolitano, "Flood mapping and impact analysis by fusion of remote sensing and open geospatial data: Sindh case study," The Egyptian Journal of Remote Sensing and Space Sciences, vol. 28, pp. 357-369, 2025.

[37] Provincial Disaster Management Authority (PDMA) Sindh, "Flood 2022 in Sindh," PDMA Sindh, 2022.

[38] C. Ruf, P. S. Chang, M. P. Clarizia, S. Gleason and Z. Jelenak, CYGNSS Handbook, Michigan Publishing, 2016.

[39] C. S. Ruf, R. Atlas, P. S. Chang, M. P. Clarizia, J. Garrison, S. Gleason, S. Katzberg, Z. Jelenak, J. Johnson and J. Sharanya , "New ocean winds satellite mission to probe hurricanes and tropical convection," Bulletin of the American Meteorological Society, vol. 97, pp. 385–395, 2016.

[40] C. S. Ruf, C. Chew, T. Lang, M. Morris, K. Nave, A. Ridley and R. Balasubramaniam, "A new paradigm in earth environmental monitoring with the CYGNSS small satellite constellation," Scientific Reports, vol. 8, pp. 1-13, 2018.

[41] C. Gerlein-Safdi and C. S. Ruf, "A CYGNSS-based algorithm for the detection of inland waterbodies," Geophysical Research Letters, vol. 46, pp. 12065–12072, 2019.

[42] S. V. Nghiem, C. Zuffada, R. Shah, C. Chew, S. T. Lowe, A. J. Mannucci, E. Cardellach, G. R. Brakenridge, G. Geller and A. Rosenqvist, "Wetland monitoring with global navigation satellite system reflectometry," Earth and Space Science, vol. 4, pp. 16–39, 2017.

[43] W. Yang, F. Guo, X. Zhang, Z. Zhang and Y. Zhu, "High temporal resolution quasi-global landscape soil freeze–thaw map from spaceborne GNSS-R technology and SMAP radiometer measurements," International Journal of Applied Earth Observation and Geoinformation, vol. 128, p. 103777, 2024.

[44] A. Tsidaev, “Parallel Algorithm for Natural Neighbor Interpolation," in Proceedings of the 2nd Ural Workshop on Parallel, Distributed, and Cloud Computing for Young Scientists, Yekaterinburg, Russia, 2016.

## Authors

**Afaq Karim** received the B.S. degree in Avionics Engineering from the Institute of Space Technology, Islamabad, Pakistan, in 2021. He is currently pursuing the M.S. degree with the School of Electronic and Information Engineering, Beihang University, Beijing, China. His research interests include GNSS-R applications for remote sensing.

**Dongkai Yang** received the B.S. degree in Electronic Engineering from North University of China, Taiyuan, China, in 1994, and the M.S. and Ph.D. degrees in Communication and Information Systems from Beihang University, Beijing, China, in 1997 and 2000, respectively. From 2001 to 2002, he was a Research Fellow with Nanyang Technological University, Singapore. Since 2010, he has been a Full Professor with the School of Electronic and Information Engineering, Beihang University. His research interests include the Global Navigation Satellite System (GNSS) and its applications.